

Hydrodynamic optimization of an axisymmetric floating oscillating water column for wave energy conversion

R.P.F. Gomes*, J.C.C. Henriques, L.M.C. Gato, A.F.O. Falcão

IDMEC, Instituto Superior Técnico, Technical University of Lisbon, Av. Rovisco Pais, 1049-001 Lisbon, Portugal

ARTICLE INFO

Article history:

Received 4 August 2011

Accepted 31 January 2012

Available online 3 March 2012

Keywords:

Wave energy

Hydrodynamic optimization using a boundary element method

Floating oscillating water column

Two-body heaving point absorber

ABSTRACT

This paper presents the geometry optimization of a floating oscillating water column (OWC). The device consists of a floater pierced by a small thickness tube open at the bottom to the sea water and at the top to the OWC chamber. The dimensions of the floater and tube are optimized in order to maximize the wave energy extraction under certain geometric constraints. The formulation considers linear water wave theory. A boundary element method code is used to calculate the hydrodynamic coefficients. The floater and the water column are assumed to oscillate only in heave. The top of the water column is modeled as a piston. The compressibility effect of the air inside the chamber is accounted for. A Wells turbine with a linear characteristic curve is considered as a power take-off system. The system is modeled in the frequency domain, assuming two degrees of freedom. The power extraction from real sea waves is simulated through a stochastic model, using an energy spectrum and the wave climate conditions off the western coast of Portugal. The dimensions of the floating OWC are optimized using two distinct optimization algorithms. Results have shown that the diameter of the floater, the submerged length and the air chamber height have a large impact on the annual average power extraction.

© 2012 Elsevier Ltd. All rights reserved.

1. Introduction

The oscillating water column (OWC) is a type of wave energy converter that has been object of study since the 1940s, when Yoshio Masuda started developing a navigation buoy powered by this device. It consists of a pneumatic chamber open at the bottom to the sea water and at the top to the outer atmosphere throughout an air turbine. The oscillating motion of the water column acted upon by waves produces a bidirectional flow through the turbine that drives a generator and produces electrical energy. The oscillatory characteristic of the flow requires the installation of a turbine and rectifying valves or, alternatively, a self-rectifying turbine. The latter option was found to be more robust and cost effective and is widely used.

The OWC concept has been extensively studied over the last thirty years. Shoreline full-scale prototypes were built in the 1980s and 1990s. These were the cases of the Kværner multiresonant OWC, Norway [1], the Pico plant in Azores, Portugal [2] and the LIMPET plant in Islay, Scotland [3]. The Pico and LIMPET plants are still operational. Those particular devices have proved the principle of operation and the extraction of energy under real sea conditions.

However, the shoreline location means a lower level of energy resource and introduces limitations into the deployment of large numbers of devices, as compared with offshore locations.

More recently, floating OWC devices have been studied and developed, namely the OE Buoy, the Orecon and the Oceanlinx Mk3 (see [4]). A 1/4th scale model of the OE Buoy device has been tested in the Galway Bay (Ireland) since 2006. The Oceanlinx Mk3 prototype was tested at an offshore location in 2010.

The self-rectifying Wells turbine has equipped most devices (Pico, LIMPET and OE Buoy). More recently, a self-rectifying impulse turbine was installed in the OE Buoy and in the Orecon device. The Oceanlinx Mk3 device was equipped with a Denniss–Auld turbine and a HydroAir variable radius turbine.

A theoretical model of the hydrodynamics of a fixed OWC device was developed by Evans [5] by considering the internal free surface as a rigid weightless piston which allowed the application of oscillating body theory. Another approach consisted in accounting for the deformation of the internal free surface through the application of an oscillating surface-pressure distribution condition [6,7]. In this way, the behavior of these devices is modeled with better accuracy, essentially when the chamber dimensions are not small compared with the wavelength. The application of this approach to particular OWC geometries was done with boundary element methods [8,9]. The modeling of the Pico power plant is presented in Brito-Melo et al. [9].

* Corresponding author. Tel.: +351218419783.

E-mail address: ruigomes@ist.utl.pt (R.P.F. Gomes).

A stochastic modeling of the OWC energy conversion device equipped with a Wells turbine was developed by Falcão and Rodrigues [10]. The same model was used to develop a control strategy to maximize the power output by controlling the rotational speed of the turbine [11] and to optimize the power-equipment considering its cost and the electrical energy extracted from different wave climates [12]. These works considered the hydrodynamics characteristics of the Pico power plant and focussed mainly on the power take-off system modeling and optimization.

The first known theoretical model of a floating OWC was formulated by McCormick [13]. Whittaker and McPeake [14] studied the effect of the floating OWC dimensions and power take-off damping in the power absorption spectrum, using a two degrees of freedom model. Recently, Alves et al. [15] developed the numerical analysis of an axisymmetric floating OWC by using a boundary element method to account for the hydrodynamic interferences between the floater and the OWC. The radiation capabilities of the floater and the effect of a deeply submerged mass (rigidly connected to the floater) were found to be important in the matching of the system dynamics to a representative incident wave frequency.

The application of optimization algorithms in the hydrodynamic design of wave energy converters has already been addressed by some authors [16–18]. Those studies yielded optimal geometrical configurations for wave energy extraction under specific conditions by the use of genetic algorithms, and were applied to two different pitching devices [16,17] and to a two-body heaving device [18].

The paper presents a method to optimize the geometry of a floating OWC restrained to move vertically. The geometry of the device is based on Falcão et al. [19], where a special shape for the tube within which the water column moves is proposed. The optimization objective is the maximization of the annual average power extracted in a wave climate at a location off the western coast of Portugal. The optimization problem is solved using two algorithms that do not require the function gradient. Several cases are computed to analyze different relations between the diameter of the floater and the total length of the device.

2. The floating OWC

The principle of operation of a floating OWC is similar to that of a fixed one. The main difference is that the structure oscillates, which consequently leads to radiation of waves. In this case, the relative motion between the device and the internal free surface provides the air flow. From oscillating body theory it is known that a system with two bodies is supposed to have two resonance peaks, due to the dynamics of each body (see [20]). If the system is tuned to have those peaks placed close to the dominant wave frequency, it is possible to widen the range of frequencies within which the system performs well. This is one of the main advantages of floating OWC devices.

This work deals with an axisymmetrical floating OWC that consists of a cylindrical floater pierced by a hollow cylinder opened at the bottom to the sea water and the top to the pneumatic chamber.

Fig. 1 presents a cross section view of the geometry. It consists of cylindrical (1, 3, 6, 8, 10 and 11), conical (2, 4, 5 and 9) and toroidal (7) surfaces and can be divided into three main parts: the floater, the small thickness tube (STT) and the large thickness tube (LTT).

The floater (surfaces 1, 2 and 11), beside producing buoyancy and enclosing the pneumatic chamber, provides (mainly through surface 2, which is facing the seabed) radiation and diffraction of waves required for efficient wave energy absorption (see [21]). Due to stability requirements, it is important to keep the mean

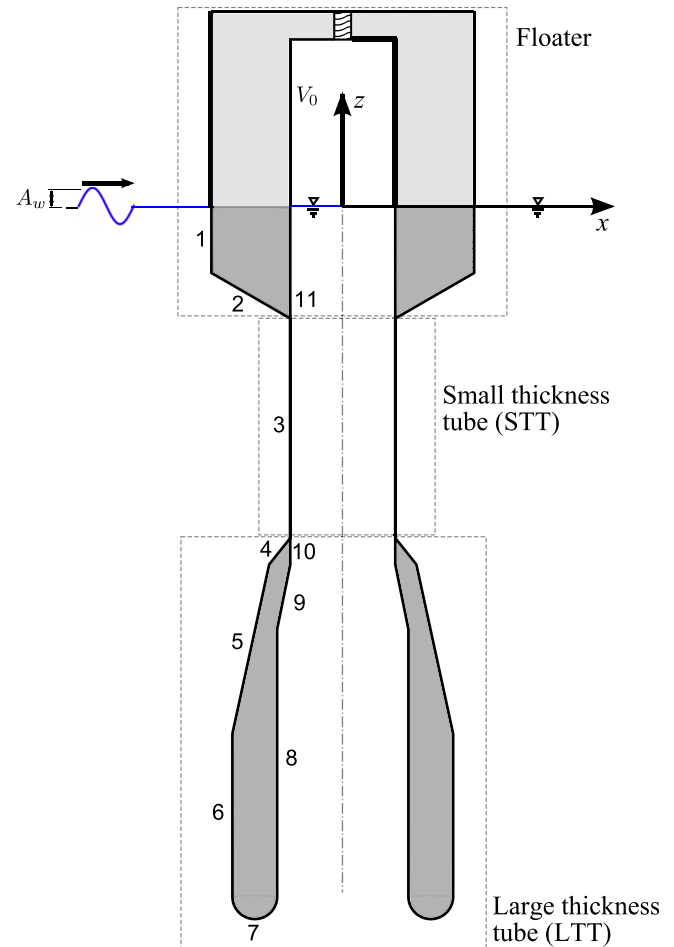


Fig. 1. Cross section view of the axisymmetric floating OWC with reference to the index of each surface.

density of the submerged part of the floater largely smaller than the water density, ρ_w .

The STT (surface 3) allows a separation between the floater and the LTT. The proximity of the LTT interferes negatively with the radiation/diffraction capabilities of the floater and therefore with the wave energy absorption. In this paper, the influence of the STT length on the energy absorption is investigated to assess the importance of this parameter.

The LTT (surfaces 4, 5, 6, 7, 8, 9 and 10) influences the inertia of the device and the inertia of the OWC. In theory, the radiation damping and diffraction force coefficients are only slightly influenced since the LTT is supposed to be deeply submerged and not to radiate nor diffract waves. The extra mass due to the presence of the submerged LTT is used to tune the device to the frequency of incoming waves. The increase in the internal diameter allows the enclosure of an additional mass of water (added mass). The toroidal surface 7 has the objective of minimizing the viscous losses in the oscillatory water flow at the bottom end of the tube. The conical surfaces 4 and 5 are used to reduce the influence of the LTT on the hydrodynamic characteristics of the floater and provide a smooth transition of diameters.

The LTT is essential for the stability of the device. By introducing a high density mass at the bottom of the LTT, the moment of inertia around the free surface (and the restoring force) in the pitching mode is maximized, and therefore the pitching stability is enhanced. If a device is supposed to oscillate in heave, it is

important to increase the distance between the centre of buoyancy and centre of gravity, to increase the pitching mode natural period and move it away from the range of periods characterizing the sea waves.

3. Theoretical model

3.1. Regular waves

The formulation presented throughout this paper considers incompressible and irrotational water flow. Linear water wave theory is applied by assuming wave amplitude and body motions much smaller than the wavelength. Since the main objective of this study is the hydrodynamic optimization, which requires intensive calculation of the linear hydrodynamic coefficients and therefore large computational time, the system was simplified by considering only two heave modes, one for the device and the other for the OWC. The top part of the OWC is modeled as a small thickness piston (rigid body) with density equal to water density. By representing the OWC top as a rigid body, the pressure on the free surface cannot be modeled as uniform. However, this is not expected to significantly affect the results of the calculations, since the diameter of the inner free surface is much smaller than the wavelength.

Consider the two-body heaving system presented in Fig. 1 where body 1 is the floater, and tube set and body 2 is the rigid piston. The time-dependent coordinates of the heaving bodies 1 and 2 are $z_1(t)$ and $z_2(t)$, respectively, increasing upwards. At equilibrium, $z_1 = z_2 = 0$.

The equations of motion can be found in [21] for an arbitrary number of oscillating bodies, and in [20] for the specific case of two bodies oscillating in heave. We consider a turbine with a linear characteristic curve (proportionality between the flow rate through the turbine and the pressure difference), which is approximately the case for a Wells turbine. The equations of motion of bodies 1 and 2, acted upon by sinusoidal waves of frequency ω , are given by

$$m_1 \ddot{z}_1(t) + \rho_w g S_1 z_1(t) - S_2 p(t) = f_{e1}(t) + f_{r1}(t), \quad (1)$$

$$m_2 \ddot{z}_2(t) + \rho_w g S_2 z_2(t) + S_2 p(t) = f_{e2}(t) + f_{r2}(t). \quad (2)$$

Here ρ_w is the water density, g is the acceleration of gravity, m_i ($i = 1$ for the floater and tube set, $i = 2$ for the piston) is body mass, S_1 is the cross sectional area of the floater defined by the undisturbed free surface, $p(t)$ is the pressure oscillation inside the chamber, S_2 is the area of the inner free surface, f_{ei} is the hydrodynamic excitation force on body i , and f_{ri} is the hydrodynamic radiation force on body i .

The mass flow rate of air through the turbine (positive for outward flow) is $\dot{m} = -d(\rho_a V)/dt$, where ρ_a is the air density and V the volume of air inside the chamber. The time-dependent volume of air is $V(t) = V_0 + (z_1(t) - z_2(t))S_2$, where V_0 is the volume of air inside the chamber in calm water. Considering air as an ideal gas and the air compression inside the chamber as an isentropic process, as proposed in [22], the mass flow rate of air through the turbine is

$$\dot{m} = \rho_a q - (V_0 + (z_1 - z_2)S_2) \frac{1}{c^2} \frac{dp}{dt}, \quad (3)$$

where q is the volume flow rate of air displaced by the relative motion of the flat free surface ($q = -S_2(\dot{z}_1 - \dot{z}_2)$) and c is the speed of sound in air. In Eq. (3), the speed of sound c and the air density ρ_a are assumed to be constant and equal to the values under atmospheric conditions. The spring-like effect of air compressibility [7]

is represented by the second term on the right hand side of Eq. (3). The effect of air compressibility increases with the average chamber height (air volume divided by the internal free surface area) and influences significantly the OWC performance when the average chamber height reaches several meters. The term $(z_1 - z_2)S_2$ will be neglected when compared to V_0 .

The performance characteristics of a turbine define the relations between the mass flow rate, the pressure difference and the power extracted and can be presented in dimensionless form (neglecting the effect of the variations in Reynolds number and Mach number (see [23])) by $\Phi = f_m(\Psi)$ and $\Pi = f_p(\Psi)$, where

$$\Psi = \frac{p}{\rho_a N^2 d_0^2}, \quad (4)$$

$$\Phi = \frac{\dot{m}}{\rho_a N d_0^3}, \quad (5)$$

$$\Pi = \frac{P_t}{\rho_a N^3 d_0^5}. \quad (6)$$

Here, N is the rotational speed (in rad per unit time), d_0 is the turbine rotor diameter and P_t the turbine instantaneous power output. For the case of the Wells turbine, it was found that f_m is approximately given by a linear relation, $\Phi = K\Psi$ [24]. Note that K is fixed for a given turbine geometry. In dimensional form, this relation is given by

$$\dot{m} = \frac{K d_0}{N} p. \quad (7)$$

Note that the dimensional damping of the turbine is given by $k = \dot{m}/p = K d_0/N$. Using Eqs. (3) and (7), we may write a linear differential equation that relates the pressure variation p and the volume flow rate q

$$\frac{V_0}{c^2} \frac{dp}{dt} + \frac{K d_0}{N} p = \rho_a q. \quad (8)$$

Since the turbine has a linear pressure versus flow rate characteristic, the system is linear and time-invariant. Then it is possible to apply a Fourier transform to the time-dependent quantities involved in the equations

$$\begin{aligned} & \{z_i, \dot{z}_i, \ddot{z}_i, p, q, f_{ei}, f_{ri}\}(t) \\ &= \text{Re} \left(\{Z_i, i\omega Z_i, -\omega^2 Z_i, \mathcal{P}, Q, A_w \Gamma_i, F_{ri}\} e^{i\omega t} \right), \end{aligned} \quad (9)$$

where Z_i , \mathcal{P} , Q , Γ_i and F_{ri} are complex quantities, Γ_i represent the linear excitation coefficient on body i and A_w is the incident wave amplitude. F_{ri} represents the frequency dependent radiation force amplitude, which is given by

$$F_{ri}(\omega) = \left(-\omega^2 A_{ii} + i\omega B_{ii} \right) Z_i + \left(-\omega^2 A_{ij} + i\omega B_{ij} \right) Z_j, \quad (10)$$

where $A_{ii}(\omega)$ is the added mass ($i = 1$ for the floater and tube set, $i = 2$ for the piston), $B_{ii}(\omega)$ is the radiation damping coefficient, and A_{ij} and B_{ij} are the coefficients concerning the hydrodynamic force on one of the bodies as affected by the motion of the other body.

Using Eqs. (1), (2), (8)–(10), and removing the time dependency, the values of Z_1 , Z_2 and \mathcal{P} can be obtained by solving the following three linear equations

$$\begin{aligned} & [-\omega^2(m_1 + A_{11}) + i\omega B_{11} + \rho_w g S_1] Z_1 + [-\omega^2 A_{12} + i\omega B_{12}] Z_2 \\ & - S_2 \mathcal{P} = A_w \Gamma_1, \end{aligned} \quad (11)$$

$$\begin{aligned} & [-\omega^2(m_2 + A_{22}) + i\omega B_{22} + \rho_w g S_2] Z_2 + [-\omega^2 A_{21} + i\omega B_{21}] Z_1 \\ & + S_2 \mathcal{P} = A_w \Gamma_2, \end{aligned} \quad (12)$$

$$\mathcal{P} = A Q, \quad (13)$$

where A is the transfer function of the pressure p frequency response to the volume flow rate q and is given by

$$A = \left(i\omega \frac{V_0}{\rho_a c^2} + \frac{K d_0}{\rho_a N} \right)^{-1}. \quad (14)$$

The volume flow rate amplitude is related to the relative motion amplitude by $Q = -i\omega S_2(Z_1 - Z_2)$.

The time-averaged value of the power available to the turbine is given by

$$\bar{P}_{\text{avai}} = \frac{K d_0}{2\rho_a N} |\mathcal{P}|^2 = \frac{k}{2\rho_a} |\mathcal{P}|^2. \quad (15)$$

3.2. Irregular waves

Irregular waves are modeled in this work following Falcão and Rodrigues [10]. It is considered that water free surface elevation of a sea state described by a frequency spectrum S_ω is a stationary stochastic process. At a fixed position, it is assumed that the water surface elevation has a Gaussian probability density function.

The variance of the free surface elevation is related to the energy density spectrum by

$$\sigma_\xi^2 = \int_0^\infty S_\omega(\omega) d\omega, \quad (16)$$

where $S_\omega(\omega)$ is a one-sided wave energy density spectrum.

Since the system is linear, the pressure oscillation $p(t)$ also has a Gaussian probability density function. We may calculate the variance of the pressure oscillations inside the air chamber as

$$\sigma_p^2 = \int_0^\infty S_\omega(\omega) \left| \frac{\mathcal{P}(\omega)}{A_w(\omega)} \right|^2 d\omega. \quad (17)$$

In the same way, the variance of the motions z_1 , z_2 and $(z_1 - z_2)$, are given by

$$\sigma_{\{z_1, z_2, z_r\}}^2 = \int_0^\infty S_\omega(\omega) \left| \left\{ \frac{Z_1}{A_w}, \frac{Z_2}{A_w}, \frac{Z_r}{A_w} \right\} \right|^2 d\omega. \quad (18)$$

The time-averaged power available to the linear turbine subject to irregular waves with a given S_ω is

$$\bar{P}_{\text{avai,irr}} = \frac{k}{\rho_a} \sigma_p^2. \quad (19)$$

Note that this equation represents the available pneumatic power and not the power converted by the turbine. The efficiency curve is required to calculate the turbine power output, as studied in [10–12].

4. Optimization technique

4.1. Computation of the hydrodynamic coefficients

The solution of the system of linear Eqs. (11)–(13) representing the dynamics of the energy extraction system requires the knowledge of frequency dependent linear hydrodynamic coefficients. The commercial boundary element method (BEM) WAMIT was used [25]. This three-dimensional panel method code, based on linear water wave theory, applies the Green's theorem to derive integral equations for the radiation and diffraction velocity potentials. Each velocity potential is represented by a distribution of singularities over the body wetted surface and verifies the linearized free surface condition and the bottom boundary condition (for constant water depth).

Two types of singularities are used to describe the velocity potential over a body surface: sources and dipoles. Sources are applicable on most bodies, except when the thickness of the body is so small that the integral equations become singular. In these cases, the potential is better represented by a distribution of dipoles, which requires a different formulation of the integral equation.

The velocity potential on the body surface is represented by B-splines in a continuous manner through the use of the higher-order method. This method, in alternative to the low-order method where the source strength is constant at each panel, provides a more accurate solution. An analytical representation of the geometry was used. A routine was coded to compute each surface coordinates and derivatives, as a function of the dimensions of the floating OWC, in order to solve the integral equations. This approach provides increased accuracy for the representation of the geometry and the discretization error becomes dependent only on the number of divisions of each surface (higher-order panels).

In order to reduce computation time and since the floating OWC has axisymmetrical geometry, use was made of the symmetric relations of the velocity potentials. Two planes of symmetry were defined at $x = 0$ and at $y = 0$. Therefore, only one quarter of the geometry is generated.

The frequency dependent hydrodynamic coefficients (A_{11} , A_{12} , A_{21} , A_{22} , B_{11} , B_{12} , B_{21} , B_{22} , Γ_1 and Γ_2) were computed for 52 frequencies equally spaced between 0.205 and 2.500 rad s⁻¹ assuming the deep water condition.

Fig. 2 presents the model of the floating OWC used to simulate the flow in the BEM. As stated before, the model simulates the heave motions of two bodies, the floater-tube set and the piston. The floater-tube set is presented in grey and its geometry consists of 11 surfaces of revolution. A dipole distribution was used over surface 3 (STT). A piston of finite thickness equal to l_1 and density equal to water density was adopted (presented in blue in Fig. 2), instead of a weightless piston of zero thickness at the free surface. The adopted model was found not to significantly affect the hydrodynamic coefficients when compared with the weightless piston model. This result was expected since the enlargement of the internal tube is relatively far from the bottom surface of the piston, and therefore the flow is approximately uniform at that distance.

A problem arises when optimizing numerically a geometry that covers a wide range of shapes since the accuracy of the method strongly depends on the number of panels and on how they are distributed over the surface. For this reason, an algorithm was created to automatically distribute the panels over the surfaces of the bodies in a manner that would maintain the accuracy of the calculation (and the total number of panels, N_t) always at the same level. This grid generation algorithm uses a cylindrical coordinate parametrization at each surface. The variable N_n^t represents the tangential distribution of panels and N_n^r the radial/vertical distribution of panels on surface n . It was found, that for this

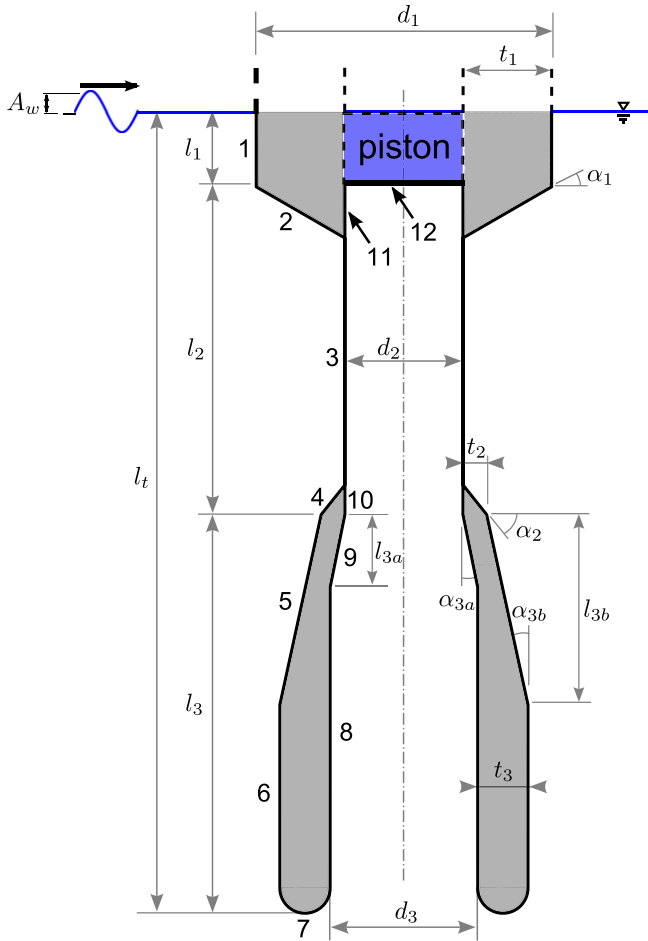


Fig. 2. Cross section view of the floating OWC model used in the BEM calculations.

axisymmetric geometry, it is important to control the parameter N_u^n in each surface to impose a regular matching of the panels in the transition of each surface. The grid generation algorithm is as follows:

1. a tangential distribution of panels on the floater-tube set (N_u^1) and piston surfaces is taken as an input variable ($N_u^1 = N_u^2 = N_u^{11} = N_u^{12}$);
2. the tangential distribution of panels on the remaining surfaces of the model is taken as half of the input value ($N_u^1/2 = N_u^3 = N_u^4 = N_u^5 = N_u^6 = N_u^7 = N_u^8 = N_u^9 = N_u^{10}$);
3. the mean radius R_m of each surface, for conical surfaces is set equal to half-sum of the maximum and minimum radii; for flat circular surfaces it is $R_m = R/\sqrt{2}$;
4. calculation of each surface generatrix length L^n ;
5. the distribution of panels in the radial/vertical direction N_v^n is given by $N_v^n = 2N_u^n L^n / (\pi R_m^n)$, N_v^n being rounded to the nearest integer;
6. minimum values of N_v^n at each surface have to be verified.

Note that the input value of the tangential distribution of panels (N_u^1) requires an even integer so that it can be halved and remain an integer.

This algorithm was applied to the discretization of every geometry hereafter. Grid convergence tests were carried out to find a good balance between the accuracy of the results and the computation time. The calculations presented in this paper

adopted $N_u^1 = 6$. Fig. 3 presents two examples of grids used in the calculations.

4.2. Optimization algorithms

In this section a brief discussion on the optimization algorithms used in this work is presented. Due to the use of a BEM to evaluate the hydrodynamic coefficients, the objective function studied in these problems is noisy, as a consequence of the numerical approximations. This means that, with very small variations in the geometry parameters, the power extraction presents small spurious oscillations. In general, optimization methods use the information on the function gradient to decide the search directions. However, in this case, the numerically computed gradient may mislead the right direction. To overcome this problem, two algorithms that do not require the evaluation of the gradient were used in the geometry optimization:

- Constrained Optimization BY Linear Approximation (COBYLA);
- Differential Evolution (DE).

The COBYLA algorithm is a direct search method developed by Powell [26]. This method uses the vertices of a simplex, as in the Simplex method (see [27]), to interpolate a linear polynomial. A new vertex is found by maximizing the linear polynomial inside a trust region with a prescribed radius and subject to the constraints of the problem. If the objective function value, at that

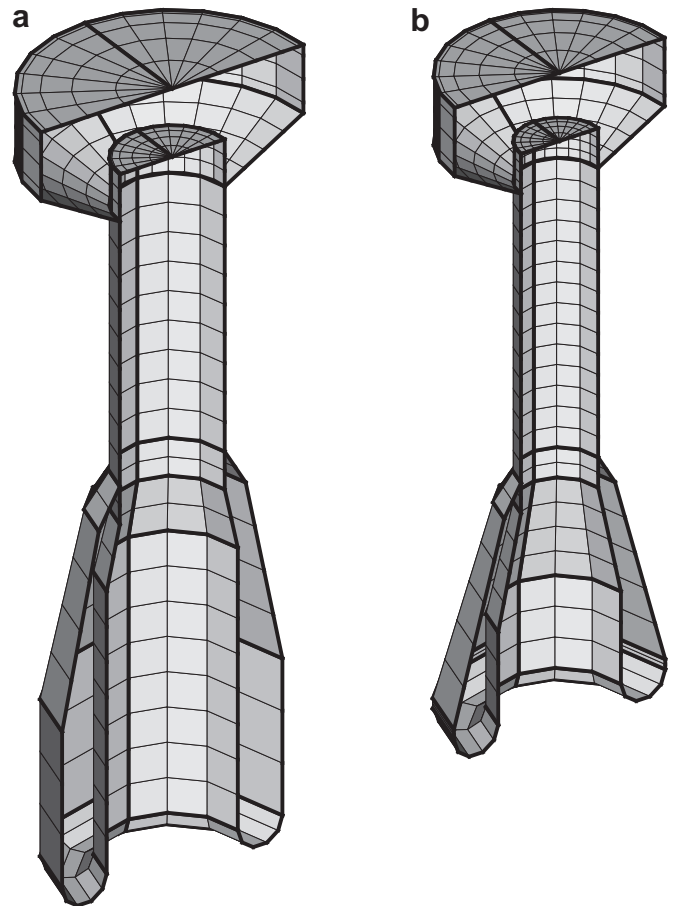


Fig. 3. Examples of two geometries discretized by the grid generation algorithm: (a) $d_1 = 20$ m, $l_t = 54.6$ m, $N_u^1 = 6$ and $N_t = 168$; (b) $d_1 = 16$ m, $l_t = 48$ m, $N_u^1 = 6$ and $N_t = 177$.

vertex, is higher than at any of the others vertices of the simplex, the vertex with the minimum objective function value is substituted by the new one. This step is repeated until convergence is found. When no improvement is verified, the radius of the trust region is reduced. Generally, convergence is found when the radius of the trust region reaches a given value, which normally defines the accuracy of the solution.

The metaheuristic DE method solves the optimization problem by iteratively improving a candidate solution through the use of genetic operations [28]. It starts by generating an initial population of N -dimensional (N being the number of optimization parameters) vectors that randomly covers the search space. For every vector of the population, a new vector is generated through mutation by applying the difference of two randomly chosen vectors to a third one. Then, some parameters of the mutated vector are randomly changed with another vector. This operation is called crossover and introduces diversity to the new vector. A greedy criterion is used to decide the new vector. This algorithm is repeated until a termination criterion is verified.

When compared with COBYLA, the DE algorithm has the advantage of a high probability of convergence to a global optimum. However it requires a much higher number of functions evaluations to converge, which results in higher computational time.

4.3. Design parameters

The objective function is represented by $F(\mathbf{v})$, where \mathbf{v} is the design vector containing the design parameters of the floating OWC. In this paper, the design vector is represented by the dimensions of the floating OWC presented in Fig. 2, with $\mathbf{v} = (l_2, d_2, l_3, d_3, t_3)$. The other dimensions of the floater remain fixed during each optimization.

Constraints on the generation of the geometry had to be created in order to avoid the generation of impossible geometries. Considering the vertical length of the conical surfaces of the LTT, l_{3a} (surface 9) and l_{3b} (surface 5), it is

$$l_{3a} = \frac{d_3 - d_2}{2 \tan \alpha_{3a}}, \quad (20)$$

$$l_{3b} = \frac{d_3 - d_2 + 2(t_3 - t_2)}{2 \tan \alpha_{3b}}. \quad (21)$$

Note that these dimensions depend on $d_3 - d_2$, therefore during the optimization process there is no direct restriction on l_{3a} and l_{3b} to be smaller than l_3 . For these cases, limiting conditions were applied. When $l_{3a} > 0.95l_3$, $l_{3a} = 0.95l_3$ and α_{3a} is calculated through Eq. (20). When $l_{3b} > 0.95l_3$, $l_{3b} = 0.95l_3$ and α_{3b} is calculated through Eq. (21).

Each design variable is subject to an upper and a lower bound. A constraint on the total submerged length of the floating OWC was added after preliminary tests showed consistently convergence to the maximum value ($l_t < l_{\max}$). This constraint was applied directly in the calculations with COBYLA. In DE, the constraint was applied indirectly through the application of a penalty function on the objective function. Whenever l_t exceeded a specified value l_{\max} , the objective function was multiplied by $(l_{\max}/l_t)^3$.

4.4. Objective function

Some preliminary designs of heaving wave energy converters are based on the energy absorption from a single wave frequency, representative of the wave climate. This normally results in a rather poor representation of the wave energy absorption spectrum,

concentrated in that design frequency. Another approach is to consider the variability of the sea waves and optimize the geometry of the device for a broader wave energy absorption spectrum (normally with a smaller peak). In the case of the floating OWC, the absorption spectrum can be enlarged by tuning the resonance frequencies of the floater-tube set and of the piston. This latter approach was adopted for the design of the objective function. Here, a wave climate off the western coast of Portugal (106 m water depth) consisting of a set of sea states was considered. Each sea state is characterized by a spectral distribution and a frequency of occurrence.

The spectral distribution is given by the one-sided Pierson–Moskowitz spectrum [29] (SI units)

$$S_\omega = 263H_s^2T_e^{-4}\omega^{-5}\exp\left(-1054T_e^{-4}\omega^{-4}\right), \quad (22)$$

where H_s is the significant wave height and T_e is the energy period. Note that the variance of the water surface elevation in Eq. (16) is $H_s^2/16$.

The frequency of occurrence ϕ at the studied location is presented by the wave climate matrix in [18] for 92 sea states ($\sum_{n=1}^N \phi^{(n)} = 1$, where N is the number of sea states). A method was used to reduce the number of sea states to 14, which maintains a good representation of the wave climate. This method reduces the number of representative sea states of a wave climate by grouping sea states, calculating equivalent H_s and T_e values and applying the conservation of the flux of energy transported by the waves in each group (see Appendix). Table 1 presents the characteristics of the 14 sea states used to represent the annual conditions. The average flux of energy E_{PM} (in kW/m) transported by the waves of a sea state described by a Pierson–Moskowitz spectrum in deep water is given by $E_{PM} = 0.4906H_s^2T_e$. The annual average flux of energy ($E_{PM,ann} = \sum_{n=1}^N \phi^{(n)} E_{PM}^{(n)}$) transported by the waves at this location is 31.37 kW/m.

The objective function of this problem was defined as the annual average power available to the turbine, computed by the weighted average of the power available to the turbine at each sea state (Eq. (19)),

$$F(\mathbf{v}) = \bar{P}_{ann} = \sum_{n=1}^N \phi^{(n)} \bar{P}_{avai,irr}. \quad (23)$$

So far, the calculation of the hydrodynamic coefficients and the derivation of average annual power were presented, but no reference was made to the values of the power take-off system parameters, namely k and V_0 . Considering a chamber of cylindrical

Table 1

Characteristics of the 14 sea states used for the calculation of the average annual power extraction.

n	$H_s^{(n)}$ [m]	$T_e^{(n)}$ [s]	$\phi^{(n)}$ [%]	$E_{PM}^{(n)}$ [kW/m]	$\phi^{(n)} E_{PM}^{(n)}$ [kW/m]
1	1.10	5.49	7.04	3.26	0.23
2	1.18	6.50	12.35	4.41	0.55
3	1.23	7.75	8.17	5.78	0.47
4	1.88	6.33	11.57	11.02	1.27
5	1.96	7.97	20.66	15.02	3.10
6	2.07	9.75	8.61	20.49	1.76
7	2.14	11.58	0.59	26.11	0.15
8	3.06	8.03	9.41	36.74	3.46
9	3.18	9.93	10.07	49.34	4.97
10	3.29	11.80	2.57	62.62	1.61
11	4.75	9.84	4.72	109.01	5.14
12	4.91	12.03	2.81	142.06	3.99
13	6.99	11.69	1.01	280.12	2.83
14	8.17	13.91	0.39	454.85	1.77

geometry, $V_0 = hS_2$, where h is the chamber height, it is necessary to guarantee that h is high enough to prevent water from reaching the turbine. The value of h was fixed.

It is known that the Wells turbine has a relatively narrow range of pressures within which it operates efficiently. We assume that the turbine has a high inertia, so that it rotates with constant velocity during each sea state and that its velocity can be controlled (and is fixed for each sea state) in order to keep the turbine at the maximum average efficiency condition (see [11]). A variation in the rotational speed results in a change in the dimensional damping of the turbine and therefore implies a change in the hydrodynamic performance, which is generally much smaller than the gain in the turbine efficiency. Now, consider that E_{PM} is only dependent on H_s^2 and that $\bar{P}_{avai,irr}$ is proportional to E_{PM} . Accepting this as a rough approximation, we may take $\bar{P}_{avai,irr}$ as being proportional to H_s^2 . Considering the performance characteristics of the turbine, in order to work always at the same conditions (same average turbine efficiency), the instantaneous power of the turbine P_t has to vary proportionally to N^3 (see Eq. (6)). The same is verified for the average power of the turbine for a given sea state $\bar{P}_t (\bar{P}_t \propto N^3)$. Under these conditions the average efficiency of the turbine $\bar{\eta}_t$ is kept constant and the following relation applies

$$\bar{\eta}_t = \frac{\bar{P}_t}{\bar{P}_{avai,irr}} \propto \frac{k^{-3}}{H_s^2}. \quad (24)$$

Introducing the control law

$$k = k_0 H_s^{-2/3}, \quad (25)$$

where k_0 is a constant, the operation of the turbine at an approximately constant efficiency is guaranteed. This result was applied in the calculations. At each evaluation of the objective function, a Newton's method was employed to compute the optimal value of the parameter k_0 . The use of an additional optimization procedure (to calculate the ideal damping applied by the power take-off system) inside the geometry optimization algorithm was previously used in [16,18].

5. Results

5.1. Geometry optimization using COBYLA

The geometry optimization using COBYLA algorithm was performed for 16 cases where the diameter of the floater d_1 and the

constraint on the submerged length (l_{max}) were varied. As stated before, 5 variables were optimized: d_2 , l_2 , d_3 , l_3 and t_3 . The objective was to maximize the annual averaged power for the wave climate presented in Table 1. In each case, bounds were applied to these variables to avoid impossible geometries. A constraint was applied in the algorithm to limit the maximum submerged length: $l_{max} > l_t = l_1 + l_2 + l_3$. Parameter l_t was limited since preliminary tests showed a consistent convergence to its maximum value.

Table 2 presents the bounds on the optimization variables, the constraint on the length and the initial values for each case optimized using COBYLA.

Preliminary tests showed that variable l_2 required always a value close to its upper bound. Therefore, the initial values were always set to a value close to their upper bound. The remaining geometrical variables had the following values:

- $l_1 = 5$ m;
- $t_2 = 0.08 d_1$;
- $\alpha_1 = 30$ deg;
- $\alpha_2 = 60$ deg;
- $\alpha_{3a} = \alpha_{3b} = 12$ deg.

If parameter l_1 were optimized, it would tend to converge to the minimum value, whereas the radiation and excitation forces would be maximized and consequently the power. In practice, this solution is not desirable since the floater may be subject to slamming, which induces high loads on the structure. Theoretically, small devices tend to have excursion larger than bigger devices. Therefore, l_1 was kept fixed for all cases. The air chamber was supposed to be cylindrical and the chamber height h was set to 10 m for all cases.

Calculations were made using an Intel Core i7 CPU 860 working at 2.8 GHz. Each function evaluation took, on average, 650 s. Each optimization case required, on average, 56 functions evaluations and 36,400 s (approximately 10 h).

Table 3 presents the summarized results of the optimizations.

Fig. 4 presents annual average power \bar{P}_{ann} absorbed by each optimized device. This result shows very well defined curves that relate the diameter and total length of the optimized device with \bar{P}_{ann} . Except for case D, a clear increase in \bar{P}_{ann} is observed with an increase in parameters d_1 and l_t .

Fig. 5 presents the non-dimensional annual average capture width $L_{c,ann}^* = \bar{P}_{ann} / (E_{PM,ann} d_1)$ for different floater diameter d_1 and submerged length l_t . It is to be noted that the capture widths for $d_1 = 16$ m are not very different from the ones for $d_1 = 20$ m.

Table 2

Description of the initial values, bounds and constraints used in each optimization case (in meters).

Case	d_1	l_{max}	d_2			l_2			d_3			l_3			t_3		
			init	min	max	init	min	max	init	min	max	init	min	max	init	min	max
A	8	24	3.20	1.60	4.80	12.88	4.08	13.68	4.00	1.60	6.40	6.12	6.00	15.60	1.36	0.76	2.36
B	8	36	3.20	1.60	4.80	19.32	6.12	20.52	4.00	1.60	6.40	11.68	9.00	23.40	1.36	0.76	2.36
C	8	48	3.20	1.60	4.80	25.76	8.16	27.36	4.00	1.60	6.40	17.24	12.00	31.20	1.36	0.76	2.36
D	8	60	3.20	1.60	4.80	32.20	10.20	34.20	4.00	1.60	6.40	22.80	15.00	39.00	1.36	0.76	2.36
E	12	24	4.80	2.40	7.20	12.88	4.08	13.68	6.00	2.40	9.60	6.12	6.00	15.60	2.04	1.14	3.54
F	12	36	4.80	2.40	7.20	19.32	6.12	20.52	6.00	2.40	9.60	11.68	9.00	23.40	2.04	1.14	3.54
G	12	48	4.80	2.40	7.20	25.76	8.16	27.36	6.00	2.40	9.60	17.24	12.00	31.20	2.04	1.14	3.54
H	12	60	4.80	2.40	7.20	32.20	10.20	34.20	6.00	2.40	9.60	22.80	15.00	39.00	2.04	1.14	3.54
I	16	24	6.40	3.20	9.60	12.88	4.08	13.68	8.00	3.20	12.80	6.12	6.00	15.60	2.72	1.52	4.72
J	16	36	6.40	3.20	9.60	19.32	6.12	20.52	8.00	3.20	12.80	11.68	9.00	23.40	2.72	1.52	4.72
K	16	48	6.40	3.20	9.60	25.76	8.16	27.36	8.00	3.20	12.80	17.24	12.00	31.20	2.72	1.52	4.72
L	16	60	6.40	3.20	9.60	32.20	10.20	34.20	8.00	3.20	12.80	22.80	15.00	39.00	2.72	1.52	4.72
M	20	24	8.00	4.00	12.00	12.88	4.08	13.68	10.00	4.00	16.00	6.12	6.00	15.60	3.40	1.90	5.90
N	20	36	8.00	4.00	12.00	19.32	6.12	20.52	10.00	4.00	16.00	11.68	9.00	23.40	3.40	1.90	5.90
O	20	48	8.00	4.00	12.00	25.76	8.16	27.36	10.00	4.00	16.00	17.24	12.00	31.20	3.40	1.90	5.90
P	20	60	8.00	4.00	12.00	32.20	10.20	34.20	10.00	4.00	16.00	22.80	15.00	39.00	3.40	1.90	5.90

Table 3
Optimization results using COBYLA algorithm.

Case	d_2 [m]	l_2 [m]	d_3 [m]	l_3 [m]	t_3 [m]	\bar{P}_{ann} [kW]	$L_{c,ann}^*$ [–]	k_0 [m ^{5/3} s]
A	3.68	12.86	4.98	6.13	2.36	43.31	0.173	0.01151
B	2.68	19.36	5.02	11.63	2.19	57.09	0.227	0.00270
C	1.77	25.92	5.89	17.08	1.33	66.91	0.267	0.00049
D	3.19	32.20	3.76	22.79	1.40	62.69	0.250	0.00208
E	5.96	12.95	7.15	6.04	3.07	77.50	0.206	0.02901
F	4.81	19.55	7.16	11.44	3.02	101.21	0.269	0.00919
G	3.67	25.44	8.91	17.55	1.81	118.27	0.314	0.00334
H	3.03	32.91	5.76	22.06	2.71	130.19	0.346	0.00105
I	9.42	12.99	9.52	6.00	3.57	113.72	0.227	0.07148
J	7.14	19.72	9.15	11.27	3.66	145.92	0.291	0.01923
K	5.88	26.34	9.35	16.65	3.37	169.17	0.337	0.00805
L	4.48	32.42	8.07	22.57	3.65	185.50	0.370	0.00283
M	11.99	12.99	11.82	6.00	4.03	149.00	0.238	0.11093
N	9.66	19.72	12.42	11.27	3.75	190.49	0.304	0.04090
O	8.18	26.35	12.35	16.64	3.45	218.17	0.348	0.01682
P	6.88	32.34	10.50	22.64	3.95	238.17	0.380	0.00739

The optimal coefficient k_0 that is proportional to k ($k = \dot{m}/p$), which defines the damping of the turbine, was analyzed for each case. Fig. 6 show the curves of the k_0 coefficient. An exponential decrease in coefficient k_0 is observed as l_t increases. This means that when compared with large l_t devices, small l_t devices require a turbine that damps much less the relative motion between the floater and the OWC. On the contrary, large d_1 devices require a turbine that damps much less than small d_1 devices.

Whittaker and McPeake [14], in their numerical modeling of a tail tube buoy, found that, in regular waves, the hydrodynamic performance improves with increasing length l_t . This agrees with the curves plotted in Fig. 4, except for point D. The same authors also found that a similar effect may be obtained by increasing the tube diameter. Note that their numerical simulations are for the range $0.75 \leq d_1/l_t \leq 1.5$. In the present paper only case M ($d_1/l_t = 0.833$) is within that range; all the others are below it. In case M (and also in case I, $d_1/l_t = 0.667$) the diameter of the water column d_2 converged to values very close to its upper bound, which agrees with their finding. However, this did not happen in most of the other cases: an increase in allowable tube length resulted in a longer and narrower OWC, see Table 3.

5.2. Geometry optimization using DE

The optimization using DE algorithm was carried out for three different cases. The three cases presented in this section, Q, R and

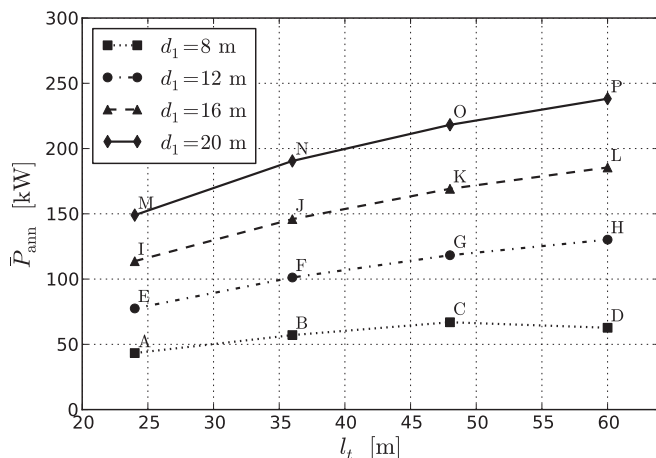


Fig. 4. Annual average power obtained for each optimization case using COBYLA.

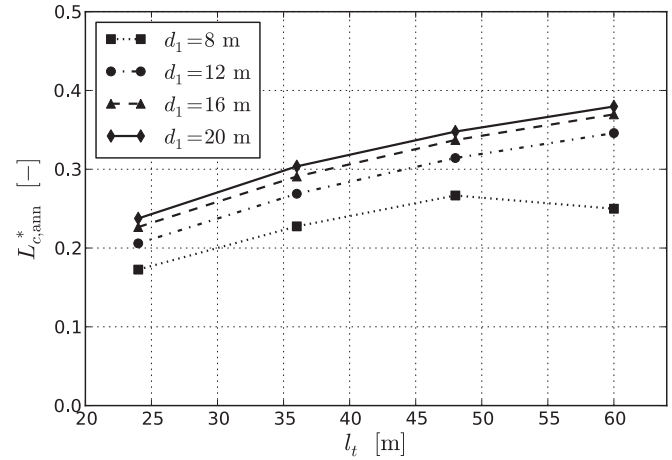


Fig. 5. Non-dimensional annual average capture width obtained for each optimization case using COBYLA.

S, are equivalent to cases A, I and K, respectively. However, these new cases do not require the initial value of the design variables to start the computation. The constraint on l_t is applied by introducing a penalty function. The factor $(l_{max}/l_t)^3$ is multiplied by the original objective function (annual average power). One objective for the use of this algorithm is to assess whether the COBYLA algorithm converged to the global maximum or to a local one.

The DE algorithm used a population of 50 vectors and was terminated after 100 generations. Each optimization case required 5000 function evaluations and approximately 903 h.

Table 4 presents the results of the optimizations with DE algorithm. Some differences are found when compared with the results from COBYLA. The major differences are found in case A and K in the parameters d_3 and t_3 . However \bar{P}_{ann} is only slightly increased, less than 1% in all cases, making COBYLA a good option when a much faster computation is required.

These small discrepancies are a result of the spurious oscillations of the objective function. When getting close to the maximum, the gradient of the function approaches zero, where the spurious oscillations become important and induce the termination criterium of COBYLA algorithm. This effect is clearly observed in Fig. 7 for cases A and Q, and in Fig. 8 for cases K and S. Those graphs consider the optimal values of l_2 , l_3 and d_2 , obtained using COBYLA and DE (approximately the same), and present the

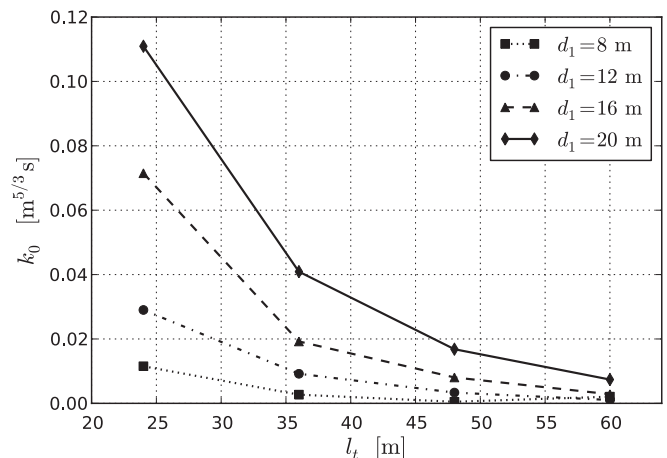


Fig. 6. Optimal k_0 coefficient obtained for each optimization case using COBYLA.

Table 4
Optimization results using DE algorithm.

Case	d_2 [m]	l_2 [m]	d_3 [m]	l_3 [m]	t_3 [m]	\bar{P}_{ann} [kW]	$L_{c,ann}^*$ [–]	k_0 [m ^{5/3} s]
Q	3.44	12.99	6.31	6.00	1.71	43.55	0.173	0.01048
R	9.60	12.99	9.72	6.00	3.40	113.92	0.227	0.07275
S	5.88	27.36	12.80	15.64	1.80	170.67	0.340	0.00859

effect of d_3 and t_3 in the annual average power. Both plots present an almost linear relation between d_3 and t_3 where \bar{P}_{ann} reaches maximum values. This is likely to be related to the effect of the inertia of the floater and OWC in the system dynamics. The plots also present the points (d_3 , t_3) given by the optimization algorithms.

5.3. Analysis of the energy absorption from each sea state

Fig. 9 presents the fractions of the average annual power extracted from each sea state. The non-dimensional capture width L_c^* of several devices when subject to the sea states that constitute the studied wave climate is presented in Fig. 10. Here, $L_c^* = \bar{P}_{ann}/(E_{PM}d_1)$. These results concern the cases where $d_1 = 16$ m. However they can be generalized to the other values of d_1 .

The sea states presented in Table 1 can be divided in four major groups. The first group incorporates sea state 1, 2 and 4. Devices with smaller l_t have a better capture width when subject to these sea states. However, their frequency of occurrence is very small and represents just a minor part on \bar{P}_{ann} . The second group embeds sea state 3, 5, 8, where T_e is within the range of 7.5–8 s. In this group, a slight increase in performance is observed as l_t increases. Sea states 5 and 8 represent a considerable part on \bar{P}_{ann} . The third group incorporates the sea states 6, 9 and 11, which have T_e within the range of 9.7–10 s. In these sea states, devices with large l_t have a very good performance. A major part of \bar{P}_{ann} is extracted from sea states 9 and 11. The forth group encloses the rest of the sea states, which have T_e within the range of 11.5–14 s. In terms of performance, these sea states contribute less than the ones in the previous group, decreasing with T_e . Since they have a small frequency of occurrence, they only have a slight impact on \bar{P}_{ann} .

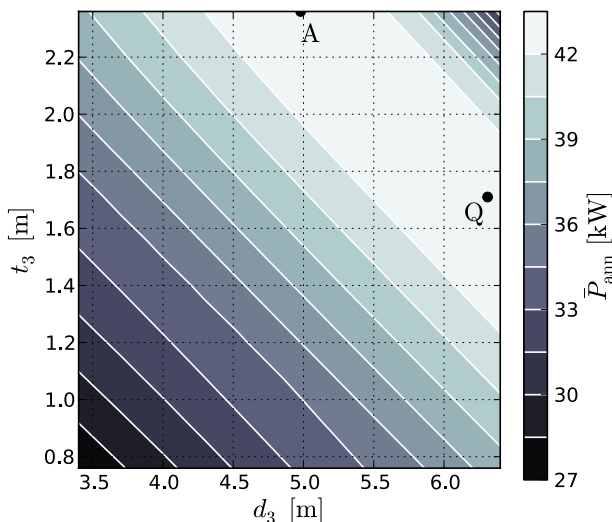


Fig. 7. Annual averaged power as a function of d_3 and t_3 , for $d_1 = 8$ m, $l_1 = 5$ m, $l_2 = 12.93$ m, $l_3 = 6.07$ m, $t_2 = 0.64$ m and $d_2 = 3.56$ m.

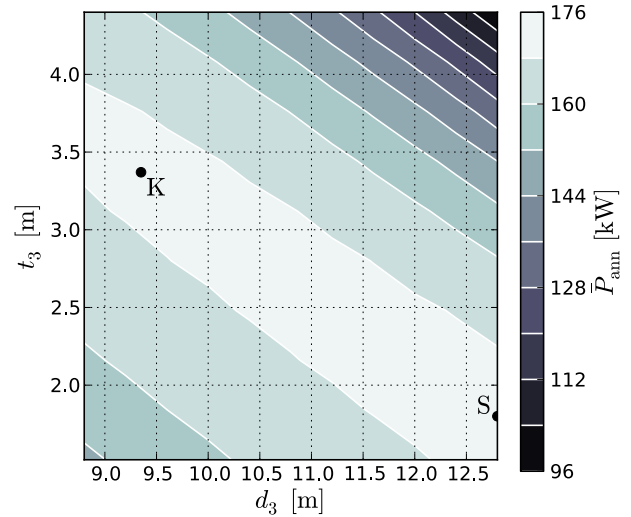


Fig. 8. Annual averaged power as a function of d_3 and t_3 , for $d_1 = 16$ m, $l_1 = 5$ m, $l_2 = 26.85$ m, $l_3 = 16.14$ m, $t_2 = 1.28$ m and $d_2 = 5.88$ m.

5.4. Discretization of the wave climate

Table 1 presents a wave climate with 14 sea states, based on a reduction of the wave climate matrix (92 sea states) presented in [18]. Using the same method it is also possible to reduce the wave climate to a single sea state represented by $H_s = 2.80$ m and $T_e = 8.14$ s. Fig. 11 presents the influence on \bar{P}_{ann} of the number of sea states (1, 14, 92) used to define a wave climate, for each optimized geometry that was obtained using the COBYLA algorithm.

As expected, a decrease in the discretization of the wave climate overestimates the \bar{P}_{ann} , due to the elimination of sea states that capture the extreme values of T_e . Due to this lack of diversity, the frequencies of incoming waves become more concentrated around values where the device performs well.

The discretization with 14 sea states was found to be a good approximation since it only overestimates \bar{P}_{ann} by 1.7%. The extreme case of only one sea state overestimates \bar{P}_{ann} by 40%.

5.5. The influence of the chamber height

In the optimizations cases, the chamber height was fixed at 10 m and the volume of the chamber only depended on d_2

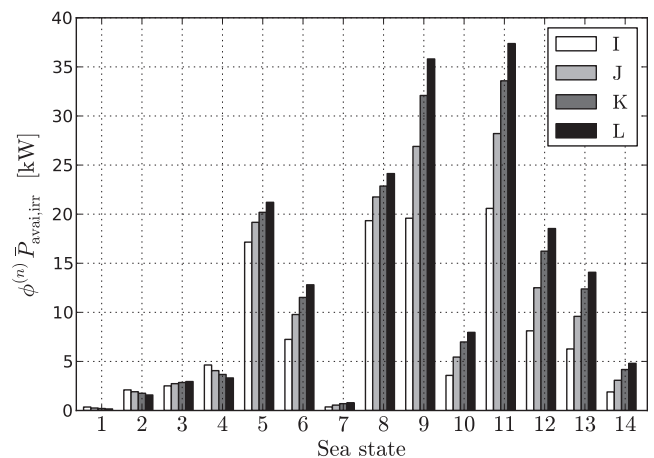


Fig. 9. Fraction of the average annual power extracted from each sea state of the wave climate given by Table 1, for the cases I, J, K and L.

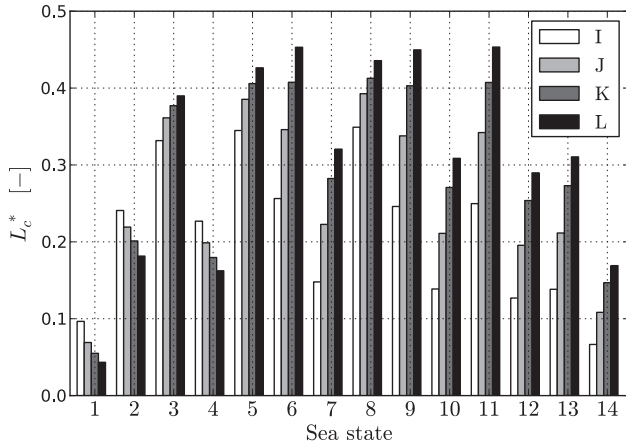


Fig. 10. Non-dimensional capture width from each sea state of the wave climate given by Table 1, for the cases I, J, K and L.

($V_0 = \pi d_2^2 h / 4$). The chamber volume is known to broaden the power absorption spectrum due to the spring-like effect of air compressibility. Fig. 12 shows how $L_{c,ann}^*$ varies with h for the cases where $d_1 = 16$ m. Each point of the graph corresponds to an optimal turbine damping k_0 . It is verified that, as l_t decreases, $L_{c,ann}^*$ become less dependent on h . For case L, where a clear influence of h on $L_{c,ann}^*$ is observed, the maximum value of $L_{c,ann}^*$ occurs for a h within the range of 10–15 m. It is also interesting to observe that the optimal situation occurs for $h \neq 0$ ($h = 0$ corresponds to incompressible flow), i.e. when a spring-like effect is introduced in the system dynamics.

A deeper analysis can be done by observing Fig. 13, where the effect of the chamber height is analyzed in the frequency domain for the cases where $d_1 = 16$ m. The power absorption spectrum of devices with small l_t is not very sensitive to the spring-like effect introduced by the increase in h . It becomes more sensitive as l_t increases. For the cases where $l_t = 48$ m (case K) and $l_t = 60$ m (case L), as h increases, the power absorption single peak (at the peak frequency) becomes smaller and forms two new peaks, one at a higher and other at a lower frequency. As these peaks increase, they move away from the central frequency, reducing the power absorption at that frequency. This effect reduces the annual average power since that central frequency is more favorable to the wave climate data used.

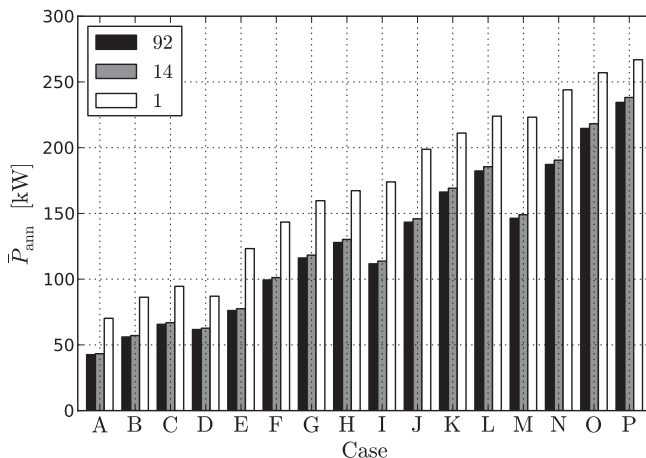


Fig. 11. Influence of the wave climate discretization on the annual average power.

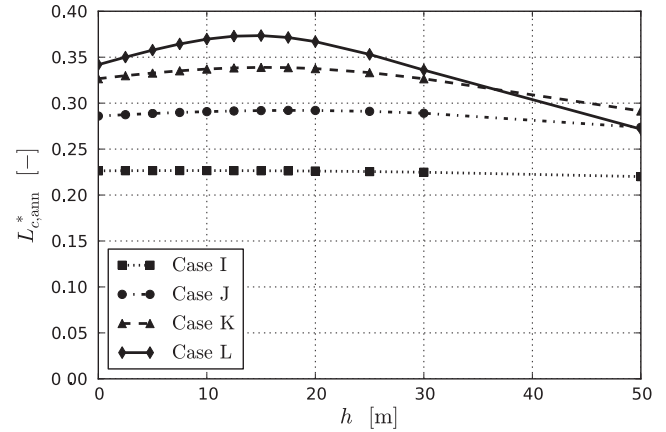


Fig. 12. The influence of the chamber height on the performance of the optimized devices, for $d_1 = 16$ m.

5.6. The influence of variations in the k_0 coefficient

The k_0 coefficient can be seen as a measure of the damping introduced by the turbine in the system dynamics. When designing a turbine to a given device, it is possible to select the turbine diameter d_0 and rotational speed N in order to match the required damping. However, those parameters are normally required to be within certain range of values. Under this condition, the required damping may not be attained and the device may be forced to work outside the range of optimal damping conditions.

Fig. 14 presents the performance of the device when equipped with turbines with different k_0 coefficients. The coefficient k_0^{opt} represents the k_0 coefficient that maximizes the annual average power for a given geometry. It is observed that increasing or decreasing by one order of magnitude the coefficient k_0 results in a very similar decrease in the annual average power, approximately 40%. Taking half or twice the coefficient k_0^{opt} , reduces the annual average power by only 4%. This may be seen as an important result since even turbines that are far from optimal damping, extract only slightly less annual energy.

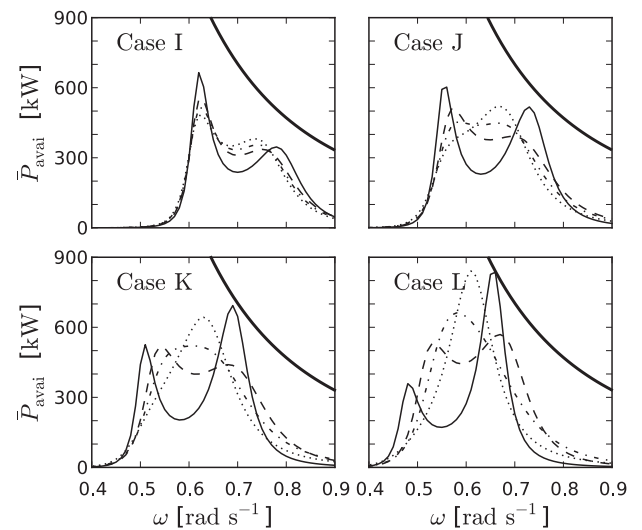


Fig. 13. Power absorption against the incident regular wave frequency, for the cases where $d_1 = 16$ m. The graphs present five curves: $h \rightarrow 0$ m (dotted line); $h = 10$ m (dash-dot line); $h = 20$ m (dashed line); $h = 50$ m (solid line); and the maximum power extraction in regular waves for an axisymmetric device in heave (solid thick line).

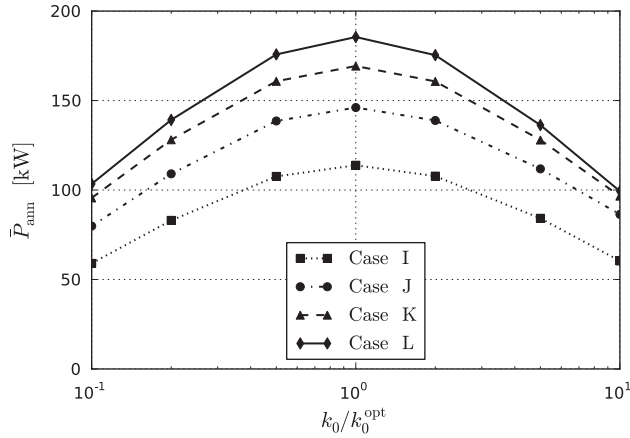


Fig. 14. Influence of deviation from the optimal damping condition on the annual average power, for $d_1 = 16$ m.

5.7. The motions of the floater and OWC

The study of the motions of the floater and OWC is an important issue to understand if the limit values are reached. The motion of the floater should always be smaller than l_1 to avoid the floater from being completely out of water. The relative motion between the floater and the OWC should never exceed h to prevent water from reaching the air turbine.

Fig. 15 presents the standard deviation values of the motion of the floater and of the relative motion between the floater and the OWC. The values are presented as a weighted average using the frequency of occurrence values of each sea state. Also the maximum and minimum values are presented. The maximum value is always obtained from the motions of the device in the more energetic sea states (high H_s), which occur very rarely.

Recalling that the motions are represented by a Gaussian distribution, a confidence interval of 99.7% is obtained if the motions are within the range of -3σ and 3σ . Even considering this high confidence interval, it is possible to observe that the motions are always below the required limits. The floater motion tends to decrease as d_1 increases, but it is not very sensitive to l_t . On the contrary, the relative motions of the OWC, which are always higher than the floater motions, seem to have a tendency to increase as l_t increases.

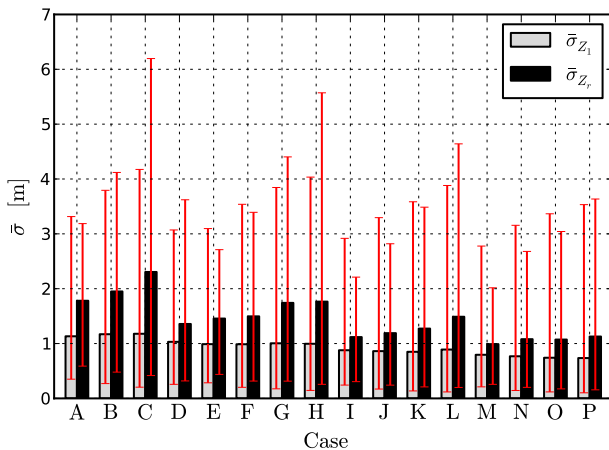


Fig. 15. Weighted average of the standard deviation of the floater motion and of the relative displacement between the floater and the OWC. The bars represent the maximum and minimum values for the given wave climate conditions.

6. Conclusion

A method to optimize the geometry of a floating OWC is presented. Several cases, considering different values of the floater diameter and total submerged length were tested in order to have a perspective on how the dimensions of the device influence the annual average power.

The distance between the floater bottom and the top of the large thickness tube part (i.e. the length of the small thickness tube) is a very important parameter because it influences the radiative capabilities of the device. In optimizations, this value tends to the upper bound value. Due to this reason, the total submerged length converged always to the upper constraint.

The study of the absorption capabilities of the device for each sea state of the wave climate showed a relationship between the total submerged length and energy period. Sea states with small energy periods tend to be more favorable for the energy absorption by devices with small total submerged length. However, these sea states with small energy period represent a very small percentage of the total energy and are always unfavorable in terms of annual average power when compared with large total submerged length devices.

For some cases with small submerged length, it was verified that the air chamber height influences only slightly the annual average power if the turbine damping coefficient is optimal. However, as the submerged length increases, the air chamber height becomes more preponderant and the maximum power absorption is found within the range of chamber height values between 10 and 20 m.

For all cases studied, it was shown that relatively large variations in the turbine damping coefficient about its optimum value have only small influence on the annual average power.

Acknowledgment

This work was supported by the funding of the Portuguese Foundation for Science and Technology to IDMEC through LAETA, and by contract PTDC/EME-MFE/111763/2009. The first author was supported by grant SFRH/BD/35295/2007 from the MIT-Portugal Program. The second author was supported through Ciência 2007 initiative. Thanks are due to Kymaner Ltd, Lisbon, for the permission to publish some of the results presented here.

Appendix A. A method to reduce the sea states of a wave climate scatter diagram

The wave climate data, in general, take a form of a wave climate scatter diagram containing the percentage of occurrence of each sea state. Therefore, each entry of the diagram represents a sea state defined by an energy period T_e and a significant wave height H_s .

In general, these data are highly discretized since they are taken from a long time series of wave surface elevation data. Numerical simulations do not require this kind of discretization in order to attain a good relation between accuracy of results and computational time. A common procedure is to reduce the entries of the scatter diagram by grouping several sea states in a representative one.

The average flux of energy of a sea state defined by a Pierson–Moskowitz spectrum in deep water, in kW/m is given by

$$E_{PM} = 0.4906 H_s^2 T_e. \quad (A.1)$$

Consider a scatter diagram as a vector ϕ_m (with a dimension M) that gives the frequency of occurrence of a sea state defined by $H_{s,m}$ and $T_{e,m}$. This method consists in assembling the M sea states into N equivalent sea states ($M = \sum_{n=1}^N M_n$) with a frequency of

occurrence ϕ_n , where the subscript n is the index of the equivalent sea state. Consider variable G_n to represent each new group and M_n its dimension. The sea states should be assembled into groups with similar probabilities, and close H_s and T_e values (containing all the non-zero values).

The equivalent sea state probability is obviously given by the sum of the probability of the group

$$\phi_n = \sum_{m \in G_n} \phi_m. \quad (\text{A.2})$$

The equivalent energy period is given by a weighted average of the periods of the group

$$T_{e,n} = \sum_{m \in G_n} \frac{\phi_m}{\phi_n} T_{e,m}. \quad (\text{A.3})$$

The equivalent energy flux transported by the waves of the group of sea states, by applying Eq. (A.1), is given by

$$E_{PM,n} = 0.4906 \sum_{m \in G_n} \phi_m T_{e,m} H_{s,m}^2 \quad (\text{A.4})$$

The equivalent significant wave height is calculated through the conservation of the energy flux

$$H_{s,n} = \left(\frac{E_{PM,n}}{0.4906 \phi_n T_{e,n}} \right)^{\frac{1}{2}}. \quad (\text{A.5})$$

This results in a vector with the (non-zero) probability of occurrence of N sea states defined by $H_{s,n}$ and $T_{e,n}$, which is an approximation to the initial wave climate scatter diagram.

References

- [1] Malmo O, Reitan A. Development of the Kværner multiresonant OWC. In: Evans DV, Falcão AF de O, editors. Hydrodynamics of ocean wave energy utilization. Berlin: Springer-Verlag; 1986.
- [2] Falcão AF de O. The shoreline OWC wave power plant at the Azores. In: Proc. 4th European Wave Energy Conference; 2000 [Aalborg, Denmark].
- [3] Heath T, Whittaker TJJ, Boake CB. The design, construction and operation of the LIMPET wave energy converter (Islay, Scotland). In: Proc. 4th European Wave Energy Conference; 2000 [Aalborg, Denmark].
- [4] Falcão AFO. Wave energy utilization: a review of the technologies. Renewable & Sustainable Energy Reviews 2010;14(3):899–918.
- [5] Evans DV. Oscillating water column wave-energy device. Journal of the Institute of Mathematics and Its Applications 1978;22(4):423–33.
- [6] Evans DV. Wave-power absorption by systems of oscillating surface pressure distributions. Journal of Fluid Mechanics 1982;114:481–99.
- [7] Sarmento AJNA, Falcão AF de O. Wave generation by an oscillating surface-pressure and its application in wave-energy extraction. Journal of Fluid Mechanics 1985;150:467–85.
- [8] Lee CH, Newman J, Nielsen F. Wave interactions with an oscillating water column. In: Proc. 6th International Offshore and Polar Engineering Conference; 1996 [Los Angeles, USA].
- [9] Brito-Melo A, Hofmann T, Sarmento AJNA, Clément AH, Delhommeau G. Numerical modelling of OWC-shoreline devices including the effect of surrounding coastline and non-flat bottom. International Journal of Offshore and Polar Engineering 2001;11(2):147–54.
- [10] Falcão AF de O, Rodrigues RJA. Stochastic modelling of OWC wave power plant performance. Applied Ocean Research 2002;24(2):59–71.
- [11] Falcão AF de O. Control of an oscillating-water-column wave power plant for maximum energy production. Applied Ocean Research 2002; 24(2):73–82.
- [12] Falcão AF de O. Stochastic modelling in wave power-equipment optimization: maximum energy production versus maximum profit. Ocean Engineering 2004;31(11–12):1407–21.
- [13] McCormick ME. Analysis of a wave energy conversion buoy. Journal of Hydraulics 1974;8(3):77–82.
- [14] Whittaker TJJ, McPeake FA. Design optimization of axis-symmetric tail tube buoys. In: Evans DV, Falcão AF de O, editors. Hydrodynamics of ocean wave energy utilization. Berlin: Springer-Verlag; 1986.
- [15] Alves MA, Costa IR, Sarmento AJNA, Chozas JF. Performance evaluation of an axisymmetric floating OWC. In: Proc. 20th International Offshore and Polar Engineering Conference; 2010 [Beijing, China].
- [16] Clément A, Babarit A, Gilloteaux JC, Josset C, Duclos G. The SEAREV wave energy converter. In: Proc. 6th European Wave and Tidal Energy Conference; 2005 [Glasgow, United Kingdom].
- [17] McCabe AP, Aggidis GA, Widden MB. Optimizing the shape of a surge-and-pitch wave energy collector using a genetic algorithm. Renewable Energy 2010;35(12):2767–75.
- [18] Gomes RPF, Henriques JCC, Gato LMC, Falcão AFO. IPS 2-body wave energy converter: acceleration tube optimization. International Journal of Offshore and Polar Engineering 2010;20(4):247–55.
- [19] Falcão AFO, Cândido JJMB, Gato LMC. Floating oscillating-water-column device for wave energy conversion. 2010. Portuguese Patent Application PT 105 171. [In Portuguese].
- [20] Falnes J. Wave-energy conversion through relative motion between two single-mode oscillating bodies. Journal of Offshore Mechanics and Arctic Engineering-Transactions of the ASME 1999;121(1):32–8.
- [21] Falnes J. Ocean waves and oscillating systems. Cambridge University Press; 2002.
- [22] Falcão AF de O, Justino PAP. OWC wave energy devices with air flow control. Ocean Engineering 1999;26(12):1275–95.
- [23] Dixon SL. Fluid mechanics and thermodynamics of turbomachinery. 4th ed. London: Butterworth; 1998.
- [24] Gato LMC, Falcão AF de O. On the theory of the Wells turbine. Journal of Engineering for Gas Turbines and Power-Transactions of the ASME 1984; 106(3):628–33.
- [25] Lee CH, Newman J. Computation of wave effects using the panel method. In: Chakrabarti S, editor. Numerical models in fluid-structure interaction. Southampton, United Kingdom: WIT Press; 2005.
- [26] Powell MJD. A direct search optimization method that models the objective and constraint functions by linear interpolation. In: Gomez S, Hennart JP, editors. Advances in optimization and numerical analysis. Dordrecht: Kluwer Academic; 1994. p. 51–67.
- [27] Press WH, Teukolsky S, Vetterling W, Flannery B. Numerical recipes in C. The art of scientific computing. 2nd ed. Cambridge University Press; 1992.
- [28] Storn R, Price K. Differential evolution – a simple and efficient heuristic for global optimization over continuous spaces. Journal of Global Optimization 1997;11(4):341–59.
- [29] Goda Y. Random seas and design of maritime structures. 2nd ed. Singapore: World Scientific; 2000.